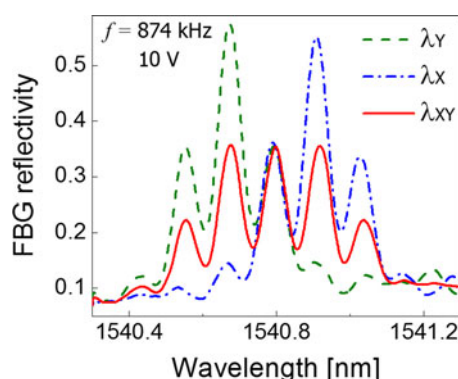🔓 **Open Access**

Electrically Tunable Multiwavelength Bragg Grating Filter Acoustically Induced in a Highly Birefringent Suspended Core Fiber

Volume 9, Number 1, February 2017

Ricardo E. Silva
Martin Becker
Manfred Rothhardt
Hartmut Bartelt
Alexandre A. P. Pohl

Electrically Tunable Multiwavelength Bragg Grating Filter Acoustically Induced in a Highly Birefringent Suspended Core Fiber

Ricardo E. Silva,[1,2] **Martin Becker,**[1] **Manfred Rothhardt,**[1]
Hartmut Bartelt,[1] **and Alexandre A. P. Pohl**[2]

[1]Leibniz Institute of Photonic Technology, Jena, 07745 Germany
[2]Federal University of Technology-Paraná, Curitiba 80230-901, Brazil

Abstract: Multiwavelength reflection spectra induced by an acoustically modulated fiber Bragg grating (FBG) in a highly birefringent suspended core fiber are experimentally investigated. Longitudinal acoustic waves interacting with a grating generate side lobes in the reflectivity spectrum and produce a superposed reflection band. The reflectivity of up to five wavelength peaks can be actively tuned by the voltage of the electrical signal inducing the acoustic waves. This indicates new possibilities for compact and fast multiwavelength dynamic and fiber-integrated reflection filters.

Index Terms: Acousto-optic devices, microstructured fibers, fiber Bragg gratings (FBGs).

1. Introduction

Fiber Bragg gratings (FBGs) inscribed in birefringent optical fibers have attracted significant interest because of their potential application as multi-wavelength reflection filters in fiber-optic systems such as fiber sensors and fiber lasers [1]–[6]. In particular, single- or dual-wavelength fiber lasers being tuned by a polarization controller have been proposed [5]. Two cascaded cavities with two high birefringent (Hi-Bi) gratings have been employed to achieve a four-wavelength laser output by adjusting the polarization losses, the pump power and the fiber length [6]. Also, a six-wavelength output fiber laser using one grating in a few-mode Hi-Bi elliptical core fiber has also been reported [7].

Although the proposed techniques to achieve multi-wavelength filtering have been successfully demonstrated, the use of conventional polarization controllers alone does not provide dynamic and fast tuning of the wavelength channels, since such devices usually are limited in their possibilities to change their spectral reflection properties. Moreover, the combination of cascaded Fabry-Perot cavities or of a high number of gratings may induce high insertion losses and increase the number of components, device size, and costs.
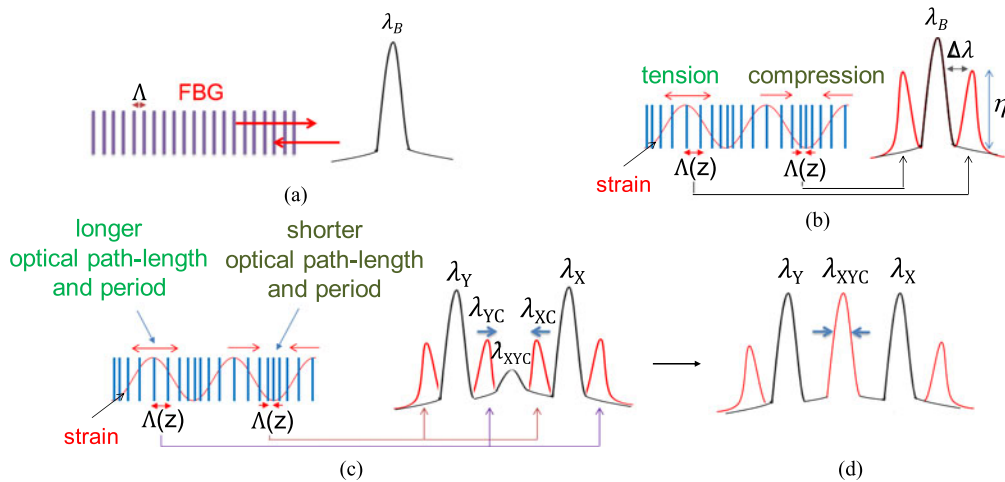
Fig. 1. Reflection spectrum of an FBG (a) without and (b) with longitudinal acousto-optic modulation in a standard single-mode fiber. Reflection spectrum of an FBG in a highly birefringent optical fiber (black line) indicating the (c) induced side lobes and the (d) superposed central lobe (red line).

On the other hand, the modulation of Bragg gratings by means of longitudinal acoustic waves enables fast electrical tuning of the grating's reflectivity and wavelength, which is suitable for optical modulators, dynamic filters and fiber lasers [8]–[12]. Fig. 1 illustrates this acousto-optic interaction. Fig. 1(a) illustrates the reflection spectrum of a non-perturbed FBG of period Λ, in a standard single-mode fiber. The power of an optical mode with effective index n_{eff} interacting with the grating is reflected at the Bragg wavelength $\lambda_B = 2n_{eff}\Lambda$. Fig. 1(b) illustrates the acoustically induced strain modulating the grating period $\Lambda(z)$ along the fiber axis z, which induces reflection side lobes on both sides of the main Bragg resonance. The side lobe reflectivity η is given as [8], [9]

$$\eta = \tanh^2 \left[\frac{\pi \Delta n_{ac} \Gamma}{\lambda_B} L_g J_m \left(\frac{\lambda_L}{\Lambda} \sqrt{\frac{2P_{ac}}{YA_S V_{ext}}} \right) \right] \tag{1}$$

in which J_m is the Bessel function of the first kind of order m, Δn_{ac} is the grating index modulation amplitude, L_g is the grating length, λ_L is the acoustic period, Γ is the confinement factor, P_{ac} is the acoustic power, Y is the Young's modulus, A_s is the silica fiber cross section, and v_{ext} is the extensional acoustic velocity in silica. The side lobe separation $\Delta\lambda$ is described as $\Delta\lambda = f \lambda_B^2 / 2n_{eff} v_{ext}$ [8]. In such a case, the acoustic wave couples power from the Bragg resonance to higher order side lobes, modulating the lobe reflectivity η and separation $\Delta\lambda$ by the acoustic power P_{ac} and frequency f, respectively.

An optical fiber with linear birefringence supports two polarization modes propagating in the core with distinct effective indices and phase velocities. The mode with the smaller effective index n_{effY} is usually named as "fast Y" mode, propagating with a higher phase velocity $v_Y = c/n_{effY}$, compared to the velocity $v_X = c/n_{effX}$ of the "slow X" mode. The interaction of these orthogonal modes XY with a grating results in two reflected bands centered at the wavelengths λ_Y and λ_X, being separated according to $\Delta\lambda_{XY} = 2\Delta n_{effXY}\Lambda$, in which Δn_{effXY} is the modal effective index difference between the modes.

The fiber/grating may also support degenerated polarization modes XYC, which propagate in phase overlapping the grating reflectivity at a resonant wavelength λ_{XYC}. Fig. 1(c) and (d) illustrates the reflected spectrum from the polarization peaks (λ_Y) and (λ_X) and a superposed central lobe (λ_{XYC}) in a highly birefringent optical fiber (black line).

Therefore, the acoustic wave may induce up to four additional wavelength reflection peaks if the peak separation $\Delta\lambda_{XY}$ is large enough to prevent the overlapping of the inner left (λ_{XC}) and inner right (λ_{YC}) side lobes, as illustrated in Fig. 1(c). Note that the modulated power reflection from
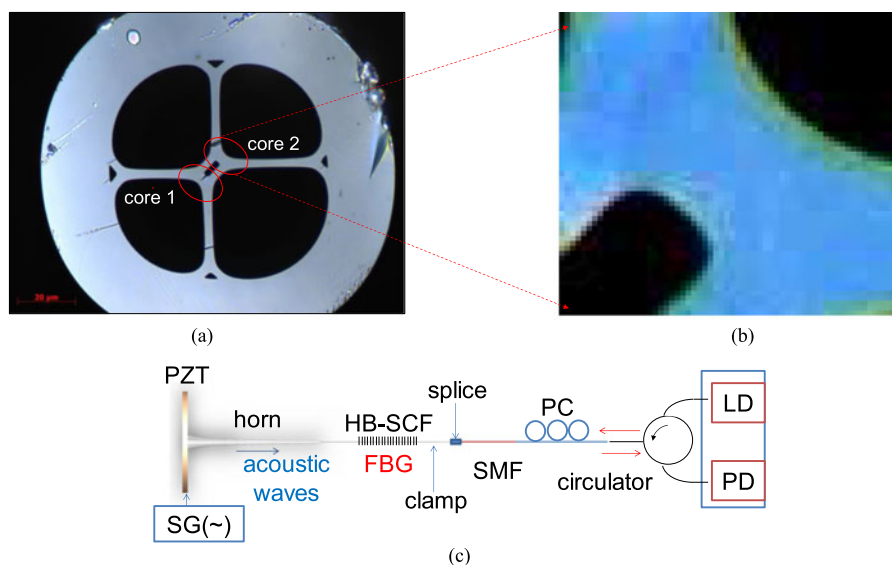
Fig. 2. (a) Cross section image of the highly birefringent double-core suspended-core fiber with a (b) detail of one core. (c) Experimental setup used to characterize the modulated FBG spectrum.

the fast mode propagates in a longer optical path length and longer grating period compared to the slow mode, which may compensate the velocities of the polarization modes to match them in phase with a degenerated mode (see Fig. 1(d)). Thus, the side lobes can be tuned by the acoustic frequency to superimpose the reflectivities of the polarization peaks so as to have a superposed central lobe at λ_{XYC}, resulting in a five-wavelength tunable reflection filter as illustrated in Fig. 1(d). The filter characteristic would be optimal to obtain six-wavelength reflection peaks if the inner left (λ_{XC}) and inner right (λ_{YC}) side lobes are equally separated between them and with the polarization peaks X and Y. Consequently, the optimal fiber birefringence $\Delta n_{eff\,fXY}$ or the acoustic frequency f might be estimated from $\Delta\lambda_{XY} \sim 3\Delta\lambda$, considering the separation of the polarization peaks, $\Delta\lambda_{XY} = 2\Delta n_{effXY}\Lambda$, and the side lobe separation, $\Delta\lambda = f\lambda_B^2/2n_{eff}v_{ext.}$ This approach might also be useful for the design of the fiber/modulator parameters for a filter with five-wavelength reflection peaks considering $\Delta\lambda_{XY} \sim 2\Delta\lambda$.

Note in (1) that for a specific value of P_{ac}, the reflectivity η is increased by reducing the fiber cross section A_s. In a standard single-mode fiber, the acoustic power is uniformly distributed over the whole fiber cross section, reducing the overlap between the acoustic power and the FBG in the core. One option to increase the acousto-optic interaction is the use of suspended-core fibers (SCFs) [13]–[15], which are generally composed of a very small core surrounded by a ring of large air holes. This significantly reduces the silica in the cladding, enhancing the acousto-optic interaction in the core [16], [17].

In the following sections, the interaction of a Bragg grating and longitudinal acoustic waves in a highly birefringent double-core suspended-core fiber (HB-SCF) is experimentally investigated. The acoustically induced superimposition of the polarization wavelength peaks resulting in a superposed reflection provides a new concept for dynamic fiber-integrated multi-wavelength optical filters.

2. Experimental Setup

Fig. 2(a) and (b) show the cross section of the highly birefringent double-core suspended-core fiber (HB-SCF) used in the experiment. The fiber is composed of a rectangular pure silica region (~14 μm length × 7.7 μm width) with a central air hole (~6 μm length × 2 μm width) surrounded by four air holes of ~40−43 μm in diameter separated by silica bridges of ~2.7 μm thickness. The
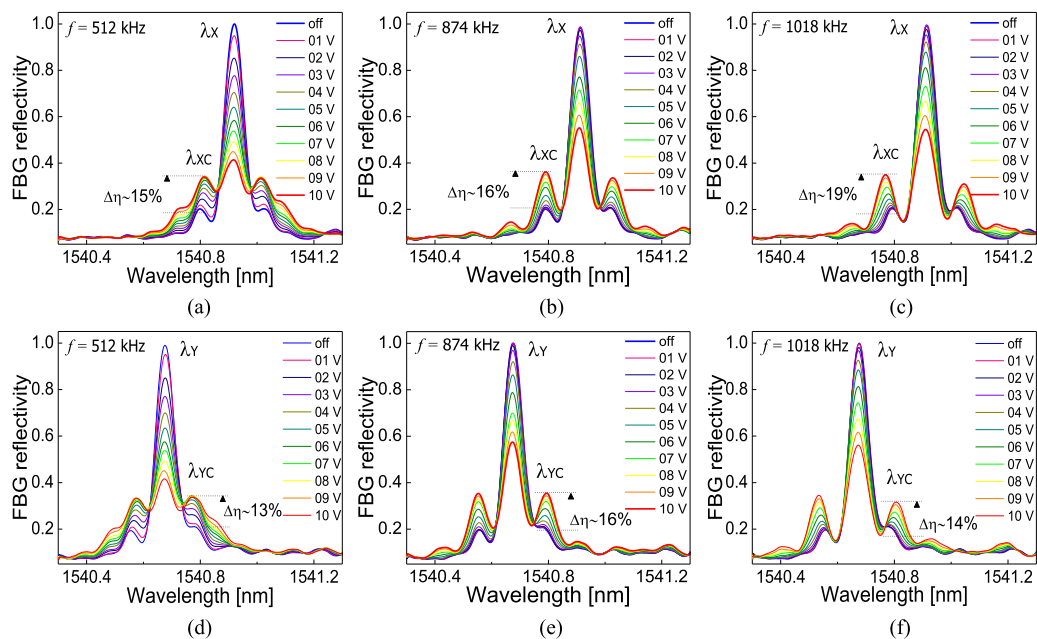
Fig. 3. FBG spectra for the grating without and with acoustic modulation for the polarizations X and Y at (a), (d) $f = $ 512 kHz; (b), (e) $f = $ 874 kHz; and (c), (f) $f = $ 1018 kHz, and a voltage range of 1 V–10 V applied to the PZT.

fiber diameter is ~124 μm. The central air hole forms two similar birefringent cores, as shown in Fig. 2(a). A detail of a core is seen in Fig. 2(b).

We inscribed a 1 cm long FBG in the HB-SCF by means of a femtosecond laser and two-beam interference, using a phase mask interferometer according to the method described in [18]. The birefringence of the HB-SCF is estimated from the polarization peaks in the grating reflection spectrum as $\Delta n_{\text{effXY}} \sim 2.2 \times 10^{-4}$.

Fig. 2(c) illustrates the setup used in the experiment. The acousto-optic modulator is composed of a piezoelectric transducer (PZT) (disc of 25 mm diameter and 2 mm thickness), a 5 cm long acoustic silica horn and a 4.4 cm long HB-SCF with the inscribed grating. The HB-SCF and the single mode fiber (SMF) connecting the circulator are aligned, and the coupling power is monitored in transmission by means of a power meter. The SMF core is aligned only to one core of the HB-SCF, since the simultaneous power coupling to the two HB-SCF cores would induce high insertion losses. The fibers are spliced using an arc-discharge fusion splicer (Sumitomo F36).

The PZT is excited by a 1 V–10 V sinusoidal signal of a signal generator (SG) at the resonances of $f = $ 512 kHz, $f = $ 874 kHz and $f = $ 1018 kHz. The mechanical deformations of the transducer are amplified by the acoustic horn into longitudinal acoustic waves interacting with the grating. A polarization controller (PC) is employed to align the polarization directions to the fast (Y), slow (X) and XY axes of the HB-SCF (XY indicates an angle of 45° between the orthogonal polarization modes). The modulated spectrum is characterized with a wavelength resolution of 1 pm for both polarizations by the Agilent 8164A Lightwave Measurement System, which is composed of a tunable laser diode (LD) and an integrated photodiode (PD).

3. Results and Discussion

3.1. Fiber Bragg Grating Reflectivity Modulation for the Polarization Peaks

Fig. 3 shows the FBG spectra for the polarizations X and Y with acoustic excitation at the resonances in the voltage range of 1 V–10 V applied to the PZT. The data are normalized to the maximum grating reflectivity in linear scale.

As expected, the acoustic wave induces reflection side lobes on both sides of the polarization wavelength peaks. The reflectivity at the peaks $\lambda_X \sim 1540.9$ nm and $\lambda_Y \sim 1540.7$ nm is modulated similarly for a maximum 10 V up to $\Delta\eta \sim 57\%$ at $f = 512$ kHz, $\Delta\eta \sim 42\%$ at $f = 874$ kHz and $\Delta\eta \sim 44\%$ at $f = 1018$ kHz, compared to the non-modulated grating. It indicates higher modulation efficiencies compared to previous studies employing standard single-mode fibers, considering similar resonances and modulation depth $\Delta\eta$ (here, the 1 cm grating is 50% shorter and the maximum voltage of 10 V is ~75% lower) [19]. The modulation depth $\Delta\eta$ variations for the considered resonances are due to the distinct deformation behavior of the PZT modes, which is explained in detail in [20]. The modulated spectra in Figs. 3(a)–(f) also indicate the coupling from the first-order side lobes to second-order side lobes, as seen in Fig. 3(a) and (d). A frequency increase from $f = 512$ kHz to $f = 1018$ kHz is useful to increase the side lobe separation.

The reflectivities of the left (λ_{XC}) and right (λ_{YC}) side lobes are indicated in Figs. 3(a)–(f) for the polarizations X and Y, respectively. Note that for both polarizations, the modulated spectra have almost the same profile. However, at $f = 512$ kHz and $f = 1018$ kHz, the reflectivities of the left and right lobes slightly differ. As illustrated in Fig. 1(b), this might be caused by a difference of positive and negative strains interacting with the grating length, since a longer region of acoustic compression than tension induces a higher reflectivity at the left side lobes for the resonances of $f = 512$ kHz and $f = 1018$ kHz.

The 3-dB bandwidth of the polarization peaks X and Y are 75 pm and 73 pm, respectively. The reflectivities of the modulated side lobes have shown similar values. This is expected for the modulation of weak Bragg gratings in which the modulated bandwidth only depends on the grating length L_g and modal effective index n_{eff}, as given by $BW = 1.39\lambda^2/\pi L_g n_{eff}$ [8].

3.2. Analysis of the Acoustically Induced Reflectivity Superposition

Figs. 4(a)–(c) show the modulated FBG spectra for the XY-polarization with 45° between the orthogonal modes (the polarization peaks are represented by λ_{XY}), for the considered resonances and voltage range. Note that the non-modulated grating has a low reflectivity superposed lobe centered at $\lambda_{XYC} \sim 1540.8$ nm, which is separated from the peaks by up to $\Delta\lambda \sim 120$ pm. This central reflection band indicates the reflection of degenerated modes at this wavelength, superimposing the reflectivities of polarization peaks X and Y. Figs. 4(d)–(f) show the comparison of the modulated spectra for the polarizations X, Y and XY and resonances at the highest voltage 10 V. It allows verifying the variation of the superposed reflectivity with the increasing frequency. Note in Fig. 4(d) for the resonance of $f = 512$ kHz, that the side lobes separation $\Delta\lambda \sim 100$ pm does not reach the coupling wavelength at $\lambda_{XYC} \sim 1540.8$ nm. Consequently, the side lobes partially overlap, decreasing the modulation depth of the superposed lobe to $\Delta\eta_{XYC} \sim 11\%$ compared to the side lobes λ_{XC} and λ_{YC}, previously shown in Fig. 3(a) and s(d), respectively.

Then the frequency is intentionally tuned at $f = 874$ kHz to match the side lobes at the coupling wavelength λ_{XYC}. Fig. 4(e) shows that the central lobe has almost the same size for both polarizations, resulting in a high total reflectivity of the overlap. The peaks of the fast, slow and superposed lobes achieve almost the same reflectivity at 10 V, with a maximum modulation depth of $\Delta\eta_{XYC} \sim 16\%$. However, it is expected that the application of voltages higher than 10 V further increases the reflectivity of the superposed central lobe with the double of the reflectivity of the right and left side lobes, reaching a saturation level at a specific voltage. The reflectivity variation slopes in Fig. 5 indicate that the reflectivity of the all wavelengths peaks follows an approximate hyperbolic function, as given in (1). A prediction of the reflectivity variation for higher voltages might be further calculated by employing the methodology described in [16]. On the other hand, the frequency detuning might overlap partially the left and right side lobes decreasing the reflectivity of the superposed central lobe, as shown in Fig. 4(f). After the detuning, a voltage increase higher than 10 V might flatten the reflectivity of the five peaks to contribute equally during the filtering. This procedure has been limited in the experiment because of the maximum 1 MHz PZT resonance frequency and the maximum voltage of 10 V of the signal generator used.
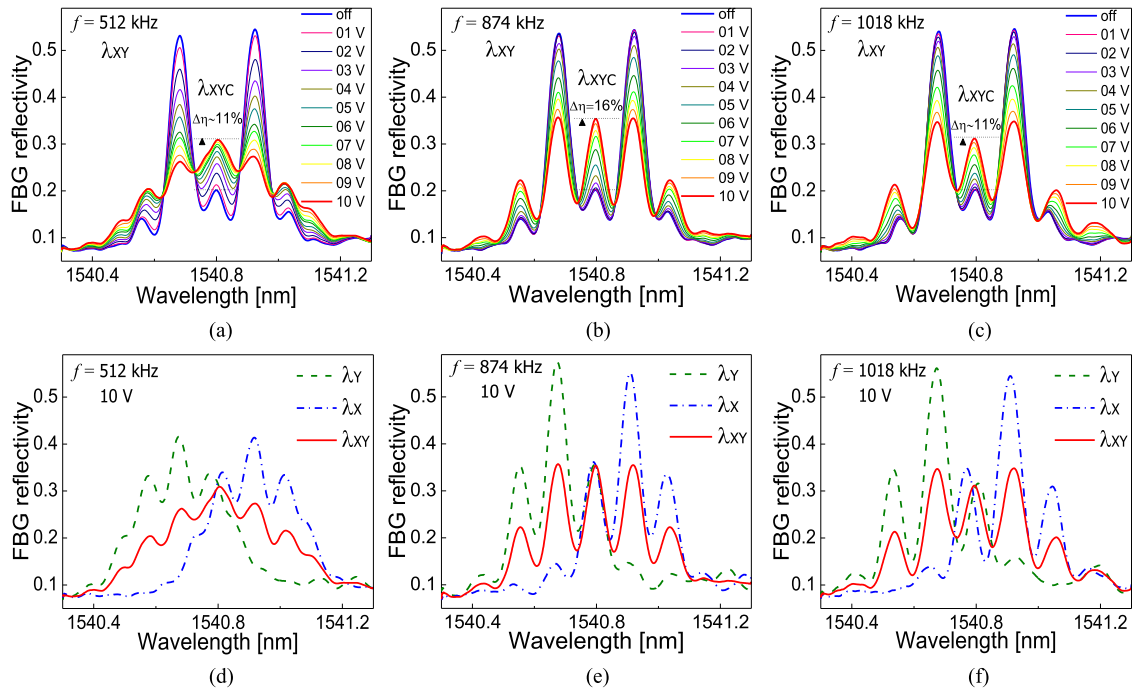
Fig. 4. FBG spectra for the grating without and with acoustic modulation for XY polarization at the resonances of (a) $f = 512\,\text{kHz}$, (b) $f = 874\,\text{kHz}$, and (c) $f = 1018\,\text{kHz}$ and the voltage range of 1 V–10 V applied to the PZT. (d)–(f) Comparison of the modulated spectra for polarizations X, Y, and XY and considered resonances at 10 V.
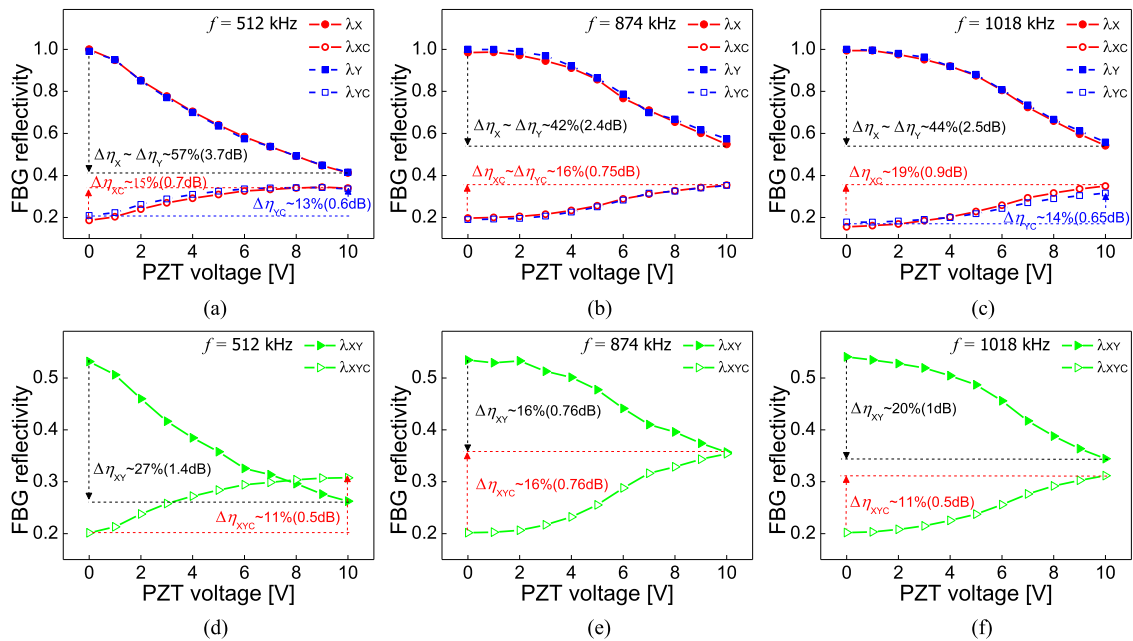

Fig. 5. FBG modulation voltage response for X, Y, and XY polarizations at the resonances of (a) $f = 512\,$ kHz, (b) $f = 874\,$ kHz, and (c) $f = 1018\,$ kHz for the voltage range of 1 V–10 V.
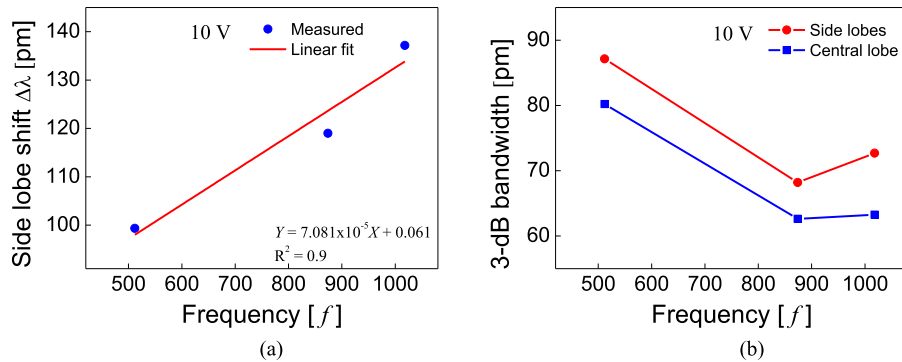
Fig. 6. (a) Averaged side lobe separation response of the X, Y, and XY polarizations at the resonances of $f = 512$ kHz, $f = 874$ kHz, and $f = 1018$ kHz at 10 V indicating a linear slope. (b) Bandwidth variation of the side lobes (red line) and central lobe (blue line) for the XY polarization and considered resonances at 10 V.

If the frequency is further increased to $f = 1018$ kHz, the lobes are shifted up to $\Delta\lambda \sim 137$ pm beyond the coupling wavelength λ_{XYC}. The lobes then overlap partially and the central lobe reflectivity is decreased ($\Delta\eta_{XYC} \sim 11\%$). It is expected that an increasing frequency above $f = 1018$ kHz might detune the side lobes entirely and suppress the central reflection to its original state. In this case, a four-wavelength dynamic filter might be implemented. The maximum side lobe separation $\Delta\lambda$ and wavelength sweep resolution are limited in this study due to the signal generator used and the discrete behavior of the resonances for the PZT employed [20].

The modulation voltage responses for the polarization reflection peaks at the three different frequencies are summarized in Fig. 5. The maximum modulation depth $\Delta\eta$ for the peaks λ_X and λ_Y, and for the induced side lobes λ_{XC} and λ_{YC} are presented in Figs. 5(a)–(c), indicating also the equivalent decibel values in brackets. Figs. 5(d)–(f) show $\Delta\eta$ at the peaks of the XY polarization λ_{XY} and the induced central lobe λ_{XYC}. The maximum side lobe reflectivity superposition is estimated by the ratio $\Delta\eta_{XYC}/\Delta\eta_{XY}$, being ∼40% at $f = 512$ kHz, ∼58% at $f = 1018$ kHz, and ∼100% at $f = 874$ kHz.

These results indicate that the side lobe reflectivity superposition is rather independent of the modulation depth for the analyzed voltage range (note that the highest modulation depth obtained is $\Delta\eta \sim 57\%$ at $f = 512$ kHz). A partial side lobe overlap created by tuning the wavelength shift is useful to adjust the strength of the reflectivity of the central, left and right lobes, e.g. for achieving the same level.

The change of the side lobe separation with the acoustic frequency is shown in Fig. 6(a). The left and right side lobe shifts of the X, Y and XY polarizations are averaged for the resonances of $f = 512$ kHz, $f = 874$ kHz and $f = 1018$ kHz at 10 V. The fit of the measured data indicates a linear response. Fig. 6(b) shows the averaged bandwidth variation of the side lobes (red line) and the central superposed lobe (blue line) for the XY polarization considering resonances at 10 V. In contrast to the modulated spectra in Fig. 3, the bandwidth of the side lobes and of the central superposed lobe for XY polarization has slightly changed compared to the original bandwidth of the polarization peaks. This change might be caused by the combination of the high variation in the side lobe reflectivity and separation. The results indicate that the increasing frequency might be useful to increase the side lobe separation, approximating the side lobes and polarization peaks to a similar bandwidth (∼75 pm at $f = 1018$ kHz). Note in Fig. 6(b) that the bandwidth of the central lobe is slightly lower for the three resonances. This indicates that a total overlap of the side lobes is also required to generate lobes with similar bandwidth. As expected, the smallest bandwidth difference between the side lobes and central lobe of 6 pm is obtained at $f = 874$ kHz.

The HB-SCF provides combined properties of highly birefringent normal fibers and suspended-core fibers. For the acousto-optic modulation of FBGs, the properties related to the suspended-core

fiber design have shown to be more relevant. Previous numerical investigations indicate that the suspended-core surrounded by the large air holes provides a larger confinement factor of the optical mode, which contributes to increase the side lobe reflectivity, as given by (1). In addition, the large air holes cause a significant reduction of the amount of silica in the fiber cross section, increasing the interaction between the acoustic wave and the grating in the core [16]. Although it is not demonstrated here, we have achieved a reflectivity modulation depth of the polarization peaks of up to 84% employing the proposed setup at $f = 289$ kHz. The high modulation depth contributes to a reduction of the grating length and the power applied to the PZT (more than 16x lower) compared to devices employing SMFs in previous studies [19]. The reduction of the fiber/grating length reduces the modulator size, which is suitable for compact and faster acousto-optic devices. Moreover, the use of the HB-SCF indicates new possibilities to increase the modulation in fibers without reducing the fiber diameter, which makes the devices more stable compared to tapering and etching techniques. It is expected that small modifications in the core dimensions of the HB-SCF can be useful to adjust the fiber birefringence without significantly affecting the benefits of the fiber design for acousto-optic modulation. In addition, the number of channels might be further increased considering the simultaneous modulation of the two cores in the same fiber.

Overall, since the proposed device is based on acoustic modulation and the "static" wave is not exactly "static," the acoustic wave will create also a modulation on the reflected signal if compared to other filters that do not work with acoustic modulation (some examples of such filters are mentioned in the introduction). In this context, modulators employing standing longitudinal acoustic waves are suitable to mode-lock all-fiber lasers inducing amplitude modulated side lobes at twice the acoustic frequency, which is beneficial to generate a pulsed laser output. This approach has also been successfully demonstrated for a mode-locked fiber laser employing a suspended-core fiber [12]. However, the narrowband wavelength modulated by the acoustic wave imposes a strong filtering in the bandwidth of the active medium, resulting in a small wavelength range (axial modes) of the gain band for mode-locking. Since the modulated bandwidth increases by reducing the grating length, the use of short FBGs is favorable to shorten the pulse width. Here, the use of a grating with 1 cm length indicates a much broader bandwidth ($\sim$74 pm) compared to previous studies with standard fibers (3.6 pm [21]). In this way, the proposed modulation of a highly birefringent suspended-core fiber indicates new possibilities for multi-wavelength pulsed fiber lasers.

4. Conclusion

The acoustically induced generation of side lobes and their reflectivity superposition from the FBG polarization peaks in a highly birefringent suspended-core fiber is shown to provide a tunable multi-wavelength spectrum for up to five wavelengths. The reflectivity of the polarization peaks and the strength of a superposed central lobe can be tuned by the voltage of an electrical signal. An optimized reflectivity superposition is achieved at $f = 874$ kHz with almost total side lobe overlapping. For frequencies in which the side lobes overlap partially, the superposed reflectivity achieves lower values.

The use of an acousto-optic modulator in combination with a polarization controller might therefore be suitable to tune from one to five wavelengths, the separation and reflectivity levels of which can be adjusted by the frequency and voltage of the acoustic modulation. It is expected that this number of channels might be further increased to 10 wavelengths considering the simultaneous modulation of the two separate cores in the same fiber as shown in Fig. 2(a).

References

[1] W. Zhang, J. A. R. Williams, and I. Bennion, "Polarization synthesized optical transversal filter employing high birefringence fiber gratings," *IEEE Photon. Technol. Lett.*, vol. 13, no. 5, May 2001.
[2] G. Chen, L. Liu, H. Jia, J. Yu, L. Xu, and W. Wang, "Simultaneous strain and temperature measurements with fiber Bragg grating written in novel Hi-Bi optical fiber," *IEEE Photon. Technol. Lett.*, vol. 16, no. 1, pp. 221–223, Jan. 2004.

[3] T. Geernaert *et al.*, "Transversal load sensing with fiber Bragg gratings in microstructured optical fibers," *IEEE Photon. Technol. Lett.*, vol. 21, no. 1, pp. 6–8, Jan. 2009.

[4] R. Leners, P. L. François, and G. Stéphan, "Simultaneous effects of gain and loss anisotropies on the thresholds of a bipolarization fiber laser," *Opt. Lett.*, vol. 19, no. 4, pp. 275–277, 1994.

[5] J. Hernandez-Cordero, V. A. Kozlov, A. L. G. Carter, and T. F. Morse, "Fiber laser polarization tuning using a Bragg grating in a Hi-Bi fiber," *IEEE Photon. Technol. Lett.*, vol. 10, no. 7, pp. 941–943, Jul. 1998.

[6] Y. Liu, X. Feng, S. Yuan, G. Kai, and X. Dong, "Simultaneous four-wavelength lasing oscillations in an erbium-doped fiber laser with two high birefringence fiber Bragg gratings," *Opt. Exp.*, vol. 12, no. 10, pp. 2056–2061, 2004.

[7] D. S. Moon, U.-C. Paek, and Y. Chung, "Polarization controlled multi-wavelength Er-doped fiber laser using fiber Bragg grating written in few-mode side-hole fiber with an elliptical core," *Opt. Exp.*, vol. 13, no. 14, pp. 5574–5579, 2005.

[8] W. F. Liu, P. S. J. Russell, and L. Dong, "100% efficient narrow-band acoustooptic tunable reflector using fiber Bragg grating," *J. Lightw. Technol.*, vol. 16, no. 11, pp. 2006–2009, Nov. 1998.

[9] P. S. J. Russell and W.-F. Liu, "Acousto-optic superlattice modulation in fiber Bragg gratings," *J. Opt. Soc. Amer. A*, vol. 17, no. 8, pp. 1421–1429, 2000.

[10] R. E. Silva *et al.*, "All-fiber 10 MHz acousto-optic modulator of a fiber Bragg grating at 1060 nm wavelength," *Opt. Exp.*, vol. 23, no. 20, 2015, Art. no. 25972.

[11] M. Delgado-Pinar, D. Zalvidea, A. Diez, P. Perez-Millan, and M. Andres, "Q-switching of an all-fiber laser by acousto-optic modulation of a fiber Bragg grating," *Opt. Exp.*, vol. 14, no. 3, pp. 1106–1112, 2006.

[12] R. E. Silva *et al.*, "Acousto-optic modulation of a fiber Bragg grating in suspended core fiber for mode-locked all-fiber lasers," *Laser Phys. Lett.*, vol. 12, no. 4, 2015, Art. no. 045101.

[13] M. C. Phan Huy *et al.*, "Three-hole microstructured optical fiber for efficient fiber Bragg grating refractometer," *Opt. Lett.*, vol. 32, no. 16, pp. 2390–2392, 2007.

[14] V. S. Afshar, S. C. Warren-Smith, and T. M. Monro, "Enhancement of fluorescence-based sensing using microstructured optical fibres," *Opt. Exp.*, vol. 15, no. 26, 2007, Art. no. 17891.

[15] L. Fu, B. K. Thomas, and L. Dong, "Efficient supercontinuum generations in silica suspended core fibers," *Opt. Exp.*, vol. 16, no. 24, 2008, Art. no. 19629.

[16] R. E. Silva, A. Hartung, M. Rothhardt, A. A. P. Pohl, and H. Bartelt, "Detailed numerical investigation of the interaction of longitudinal acoustic waves with fiber Bragg gratings in suspended-core fibers," *Opt. Commun.*, vol. 344, pp. 43–50, 2015.

[17] R. E. Silva, M. Becker, A. Hartung, M. Rothhardt, A. A. P. Pohl, and H. Bartelt, "Reflectivity and bandwidth modulation of fiber Bragg gratings in a suspended core fiber by tunable acoustic waves," *IEEE Photon. J.*, vol. 6, no. 6, Dec. 2014, Art. no. 7100608.

[18] M. Becker *et al.*, "Fiber Bragg grating inscription combining DUV sub-picosecond laser pulses and two-beam interferometry," *Opt. Exp.*, vol. 16, no. 23, 2008, Art. no. 19169.

[19] R. A. Oliveira, P. T. Neves Jr., J. T. Pereira, J. Canning, and A. A. P. Pohl, "Vibration mode analysis of a silica horn–fiber Bragg grating device," *Opt. Commun.*, vol. 283, no. 7, pp. 1296–1302, 2010.

[20] R. E. Silva, M. A. R. Franco, H. Bartelt, and A. A. P. Pohl, "Numerical characterization of piezoelectric resonant transducer modes for acoustic wave excitation in optical fibers," *Meas. Sci. Technol.*, vol. 24, no. 9, 2013, Art. no. 094020.

[21] I. L. Villegas *et al.*, "Mode-locked Yb-doped all-fiber laser based on in-fiber acoustooptic modulation," *Laser Phys. Lett.*, vol. 8, pp. 227–231, 2011.